SUPPLEMENTARY INFORMATION

Hydrocarbon Diffusion in Siliceous Chabazite: Uptake Experiments and DFT-Corrected Transition-State Modeling

Tomáš Volný [a, c], Jakub Halamek[b], Yosra Gherib[b], Roman Bulánek[b], Ota Bludský [a]

[a]Institute of Organic Chemistry and Biochemistry, Academy of Sciences of the Czech Republic, Flemingovo nám. 2, 162 10 Prague, Czech Republic

[b]Department of Physical Chemistry, Faculty of Chemical Technology, University of Pardubice, Studentská 573, 532 10 Pardubice, Czech Republic

[c]Department of Physical and Macromolecular Chemistry, Faculty of Science, Charles University, Hlavova 8, 128 40 Prague, Czech Republic

e-mail: ota.bludsky@uochb.cas.cz

Experimental

Synthesis

Si-CHA was synthesized hydrothermally using N,N,N-trimethyl-1-adamantylammonium hydroxide (TMAdaOH) as the OSDA, as described in literature.[1,2] The final gel composition was: 1 SiO_2: 0.75 TMAdaOH: 0.75 HF: 4 H_2O. The procedure itself consisted of adding 19.7 g of a 25 wt.% TMAdaOH solution (CymitQuimica) over 6.5 g of tetraethyl orthosilicate (Merck). The resulting mixture was stirred until complete evaporation of the ethanol and excess water, achieving a final H_2O/SiO_2 molar ratio of 4.0. Subsequently, 1.17 g of aqueous HF (40 wt.%) (Merck) was added, and the synthesis gel was homogenized manually before being transferred into a 45 mL Teflon-lined stainless-steel autoclave. The crystallization process was conducted at 423 K for 5 days and 14 h. The resulting solid was thoroughly washed with redistilled water, dried, and then calcined at 853 K for 8 h to remove the organic template.

Characterization

The PXRD measurement was conducted on a benchtop Rigaku MiniFlex600 diffractometer employing a silicon strip detector (D/teX Ultra) and using the CuKα radiation (λ = 1.5406 Å) (Kβ foil filter made of Ni was further employed). The experiment was performed in the Debye-Scherrer setup using a glass capillary with an outer diameter of 0.7 mm (wall thickness 0.01 mm). The obtained diffractogram featured only a single phase with no clear impurities and was subsequently optimized using the Le Bail refinement in the Jana2006 software.[3] The refinement was performed under the constraint of the $R\bar{3}m$ symmetry using the cell parameters from literature[1] as the initial values. The refinement was performed in the range of 8 to 60° 2θ. Legendre polynomials (n = 15) were used to fit the background, while the peak shape was described by the Pseudo-Voigt model along with the Bérar-Baldinozzi asymmetry correction (4 parameters were used). Sample displacement was likewise optimized. The resulting fit (see Fig. S1) was of very high quality (GOF = 1.04; R_p = 3.85 %; Rwp = 4.93 %), yielding the following values of lattice parameters: a=b=13.52386 Å; c=14.73916 Å; α=β=90°; γ=120°. These values match those from the original publication[1] to within 0.01 Å.

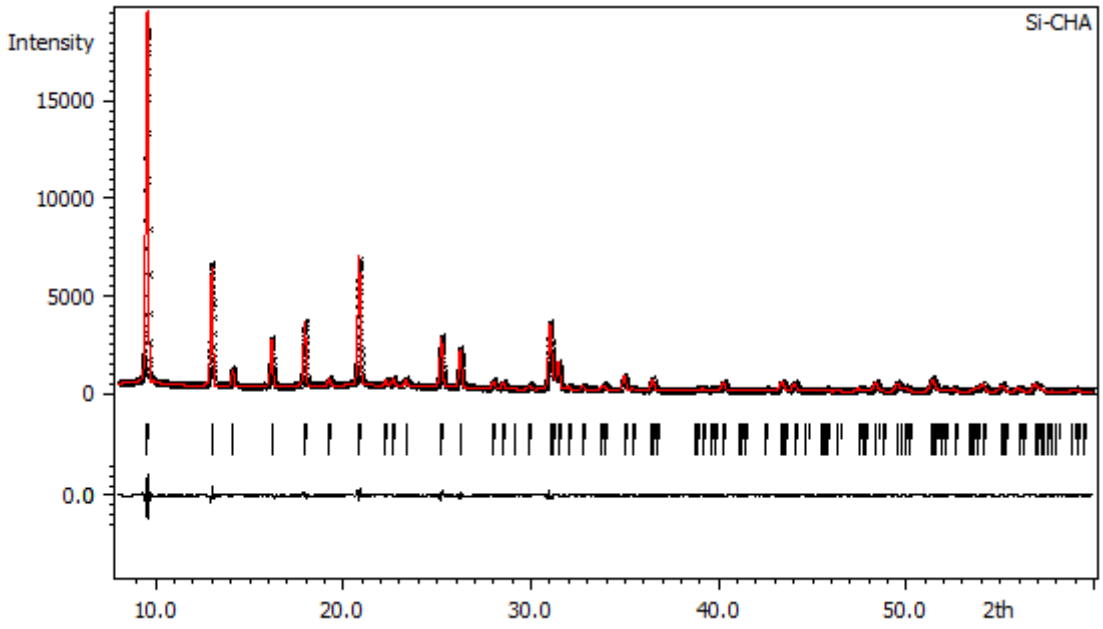


Figure S1: The PXRD pattern of the Si-CHA material, optimized by the Le Bail refinement

The N_2 adsorption isotherm (see Fig. S2) was measured at 77.3 K employing the same device (Micromeritics ASAP 2020 Plus Physisorption) as in the case of the uptake curve measurements. Prior to the experiment itself, the sample was thermally treated under dynamic vacuum at 523 K for 6 h. The obtained adsorption isotherm was a typical very steep type I adsorption isotherm according to the IUPAC classification.[4] The micropore volume (V_{mic} = 0.305 cm^3/g) and the external surface area (S_{ex} = 0.8 m^2/g) were obtained via the *t*-plot method[5] employing the Harkins-Jura master isotherm[6, 7], as per up to date IUPAC recommendations.[4]

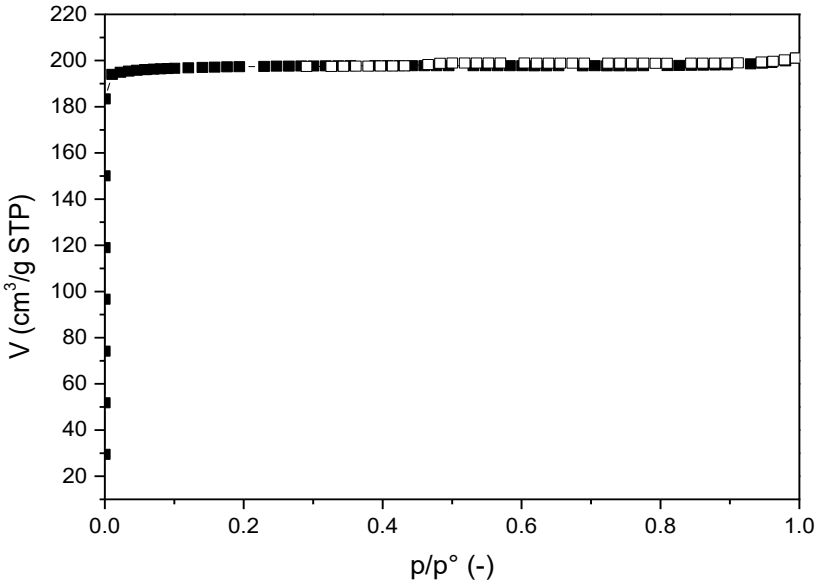


Figure S2: The N_2 adsorption isotherm (77.3 K) of Si-CHA

The SEM images (see Fig. S3) were recorded using a tabletop Hitachi TM4000Plus II instrument. The images were recorded by the BSE (backscattered electron) detector on uncoated samples using the acceleration voltage of 10 kV in the high vacuum mode. The images revealed that the sample was composed of individual rhombohedral (nearly cubic) crystals of a very narrow size distribution with occasional intergrowths, and smaller crystallites of different shapes being present.

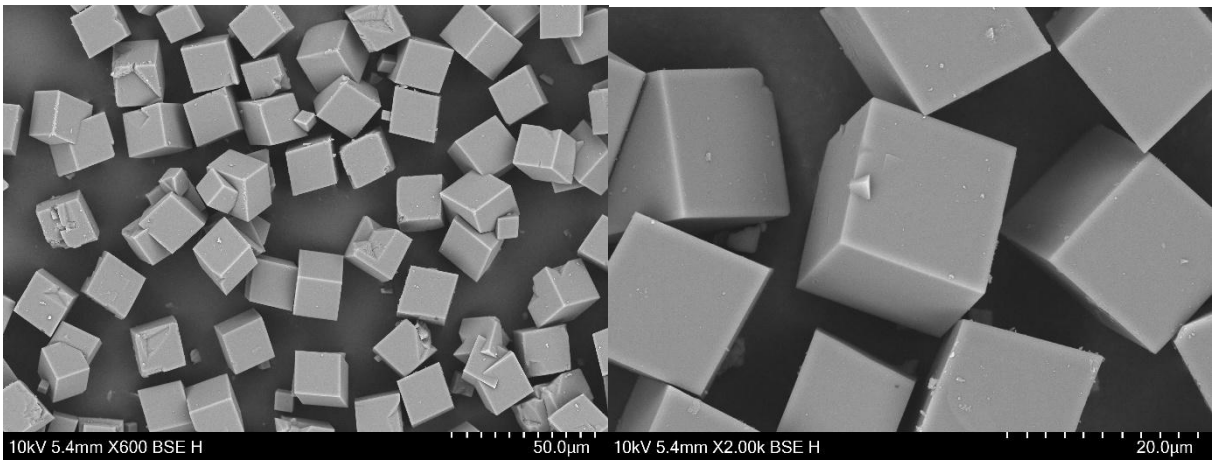


Figure S3: The SEM images of Si-CHA

The typical crystal diameter was determined to be approximately $d \approx 16$ μm (see Fig. S4 for the histogram of the obtained crystal sizes from the image in Fig. S3 on the left). This value was then employed in the calculation of the diffusion coefficients.

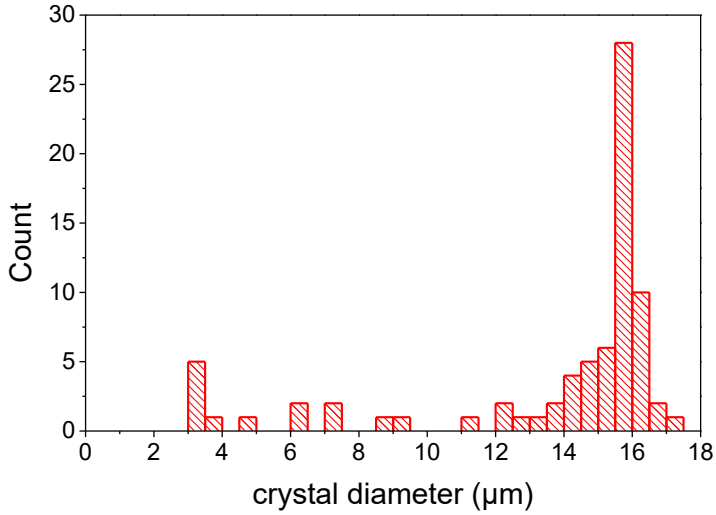


Figure S4: Histogram of the crystal diameters obtained from SEM

Uptake curve measurements

The uptake curves were measured using a commercial volumetric/manometric ASAP 2020 Plus Physisorption instrument, employing the ROA ("rate of adsorption") plugin.

The same sample batch (0.0795 g of dry sample) was repeatedly used for all the experiments (incl. the N_2 isotherm measurement, which was performed first). Prior to each uptake curve measurement, the sample was regenerated at 473 K (depending on the last measured hydrocarbon, the duration of the treatment varied from 1 to 33 hours, to ensure the full activation of the material).

The experiment itself consisted, in each case, of dosing the same quantity of hydrocarbon gas (~62.5 torr dose in a 45.4400 cm^3 large manifold tempered at ~303 K) into an evacuated sample cell (20.13 cm^3) tempered exactly at 303.15 K – the temperature was controlled by a Peltier thermostat equipped with a Pt sensor (supplied by e-Lab services, Czech Republic; temperature control accuracy ± 0.1 K). The final equilibrium pressure differed considerably for the various gases, ranging from 42.5 torr in the case of the blank experiment with the non-adsorbing He, up to ~8 torr, in case of the most adsorbing gas – (E)-but-2-ene. The blank experiment with He revealed that upon opening the valve between the manifold and the sample tube, it takes approximately 3 s for the obtained signal to fully stabilize and so the datapoints obtained within the first 3 s upon opening the valve were ignored in the evaluation.

Gases of the following purity were used for the experiments: 99.9995 % methane (supplied by Linde Gas), 99.995 % ethane (GHC), 99.9 % ethene (Linde Gas), 99.99 % propane (GHC), 99.97 % propene (GHC), 99.95 % butane (Linde), 99.6 % but-1-ene (Sigma), 99 % (E)-but-2-ene (Sigma), 99 % (Z)-but-2-ene (GHC), 99.9 % isobutane (SIAD), 99.5 % isobutene (Sigma).

Uptake curve evaluation

The simple $\sqrt{t}$-law, valid for the low-uptake limit of the uptake curve measured at isothermal conditions was employed in the evaluation[8]:

$$\frac{n(t)-n(0)}{n(\infty)-n(0)} \approx 6\sqrt{\frac{Dt}{\pi R^2}} \qquad (1)$$

In this model, $n(t)$ stands for the adsorbed amount at time t; $n(\infty)$ stands for the equilibrium uptake; $n(0)$ stands for the adsorbed amount in the sample chamber before the process, and D/R^2 stands for the apparent diffusion coefficient of the gas.

Employing the $\sqrt{t}$-law (see Fig. S5, Table S1), the diffusivity values were obtained from the initial slopes of the $\frac{n(t)-n(0)}{n(\infty)-n(0)} = f(\sqrt{t})$ curves (assuming zero intercept). For the faster adsorbing hydrocarbons (ethane, ethene, propene, (E)-but-2-ene) the experimentally obtained value of $n(\infty)$ was employed in the calculation. This value was unavailable in the case of the slowly adsorbing hydrocarbons (propane, butane, but-1-ene, (Z)-but-2-ene), and so to have a reasonable approximation, the equilibrium uptake of propene was employed when calculating the propane diffusivity, and the equilibrium uptake of (E)-but-2-ene was used in the case of the slower C_4 hydrocarbons.

Considering the nearly cubic shape of the crystals and assuming that the internal diffusion in the micropores is the driving process behind the observed mass transport, the values of diffusion coefficients were obtained from the calculated apparent diffusion coefficients D/R^2 by multiplying them by the square of the estimated value of effective radius R, calculated as $R = 3V/A = 3d^3/6d^2 = d/2 \approx 8\ \mu m$, with the value $d \approx 16\ \mu m$ obtained from the SEM images (see Figs. S3, S4).

A summary of the basic experimentally obtained parameters and of the obtained diffusivity values is in Table S1.

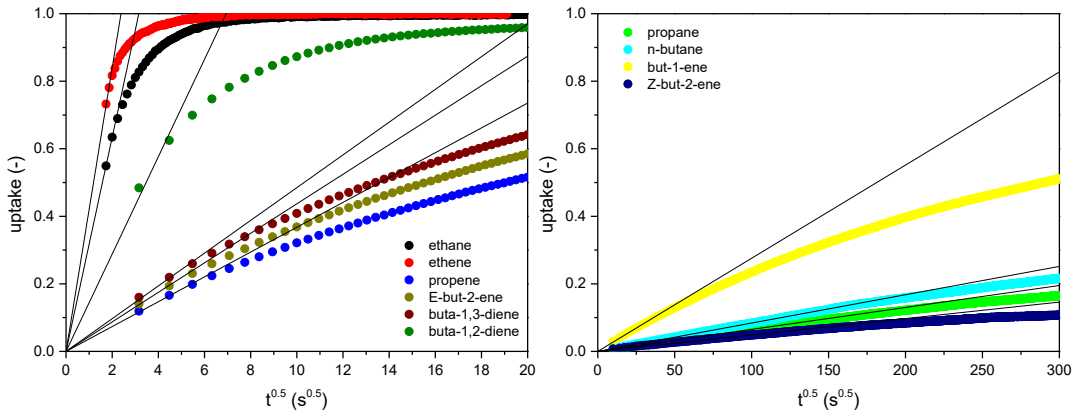


Figure S5: $\sqrt{t}$-law analysis of the hydrocarbon uptake curves

Table S1: The summary of the uptake curve measurement results sorted in descending order of diffusion coefficients.

gas	n(∞) (mmol/g)	p(∞) (torr)	slope ($s^{-0.5}$)	D/R^2 (s^{-1})	D (m^2s^{-1})

methane	0.03	41.62	-	-	-
ethene	0.28	35.71	4.20E-01	1.54E-02	**9.85E-13**
ethane	0.43	32.34	3.17E-01	8.78E-03	**5.62E-13**
(E)-but-2-ene	1.54	8.02	4.37E-02	1.67E-04	**1.07E-14**
propene	1.25	14.11	3.68E-02	1.18E-04	**7.55E-15**
but-1-ene	-	-	2.76E-03	6.65E-07	**4.25E-17**
butane	-	-	8.39E-04	6.14E-08	**3.93E-18**
propane	-	-	6.51E-04	3.69E-08	**2.36E-18**
(Z)-but-2-ene	-	-	4.86E-04	2.06E-08	**1.32E-18**

Computational

The results from nudged-elastic band (NEB) calculated diffusion coefficients are presented in the Table S2. The *fit* values were obtained from joint fit of iFF and SLC values in order to have a single D_0 pre-exponential factor. That way, only a single degree of freedom can be studied – the enthalpic contribution. The *NEB* energy barriers were calculated as difference in transition state and deepest local minima located. *Direct* diffusion coefficients come directly from transition state theory applied to free energy surfaces at 300 K. The *fit* values come from the Arrhenius equation with fitted D_0 and E_a. The *corrected* values come from the QM-MM correction scheme.

Table S2: The summary of the computational results sorted in descending order of diffusion coefficients.

	Fit			NEB		
	E_a (kJ mol^{-1})		D_0 (m^2 s^{-1})	E_a (kJ mol^{-1})		
	iFF	SLC	double fit	iFF	SLC	DFT
methane	22.7	18.5	4.0E-09	20.0	16.2	16.3
ethene	23.4	19.1	4.1E-10	18.0	14.1	15.3
ethane	26.0	21.5	2.9E-10	21.2	16.9	18.1
(E)-but-2-ene	34.9	29.9	4.9E-10	29.4	24.3	29.0
propene	36.9	30.2	1.1E-10	32.6	27.0	31.7
but-1-ene	41.3	37.8	4.0E-11	47.2	43.3	47.6
butane	50.8	42.2	2.5E-11	48.1	39.5	44.3
propane	52.5	44.2	5.2E-11	48.4	40.8	50.2
(Z)-but-2-ene	73.8	62.2	1.1E-11	70.8	58.0	44.9

	D 300 K (m^2 s^{-1})					
	direct		fit		corrected	
	iFF	SLC	iFF	SLC	iFF	SLC
methane	3.7E-13	2.1E-12	4.5E-13	2.4E-12	2.0E-12	2.4E-12
ethene	4.0E-14	2.8E-13	3.5E-14	2.0E-13	1.0E-13	1.2E-13
ethane	8.2E-15	5.0E-14	8.4E-15	5.2E-14	2.9E-14	3.3E-14
(E)-but-2-ene	4.3E-16	3.8E-15	4.2E-16	3.0E-15	4.9E-16	4.5E-16
propene	4.4E-17	4.9E-16	4.4E-17	6.3E-16	6.3E-17	9.8E-17
but-1-ene	2.4E-18	6.4E-18	2.6E-18	1.0E-17	2.2E-18	1.8E-18
butane	8.4E-20	8.6E-19	3.6E-20	1.1E-18	1.6E-19	1.7E-19
propane	3.3E-20	8.8E-19	3.7E-20	1.0E-18	1.8E-20	2.4E-20
(Z)-but-2-ene	1.2E-21	2.0E-22	1.5E-24	1.6E-22	5.0E-20	3.1E-20

Framework flexibility

This section examines the role of framework flexibility in the interactions of hydrocarbons with porous materials by means of computational modeling. Flexibility in zeolite frameworks arises from multiple sources and can substantially affect diffusion rates and energy barriers. Three primary categories of flexibility are considered in this study: geometry-induced effects, temperature-induced effects, and guest-induced effects. Incorporating these aspects into computational simulations allows for a more realistic and physically meaningful description of the material behavior under different conditions.

Geometry-induced flexibility

One of the primary characteristics of a zeolite framework is its lattice geometry. For a reliable computational approach, it is essential to accurately describe the structure of the framework. Since this study compares two force fields – iFF and SLC – individual unit cells optimized at 0 K were generated for each, as the force fields differ in their description of interatomic interactions. In order to meaningfully compare the force fields results, a common reference is needed. Therefore, the 0 K optimized structures obtained from iFF and SLC were compared with both the experimental, and the theoretical (DFT, IZA) structures.[9, 10] The corresponding lattice parameters from all four methods are summarized in Table S3, ordered by increasing volume.

Table S3: Lattice parameters for chabazite at 0 K for different methods: iFF and SLC force fields, DFT[9], IZA structure[10], and experimental published data[1]. Calculated structures ordered by increasing volume.

	$a = b = c$ (Å)	$\alpha = \beta = \gamma$ (°)	V (Å^3)
SLC	9.198	94.751	769.783
iFF	9.272	94.609	788.887
DFT	9.276	94.833	789.048
IZA	9.304	94.597	797.179
exp	9.229	94.267	779.286

The four different structures presented in Table S3 slightly differ. The SLC description yields a relatively compact framework, with a unit cell volume approximately 10 Å^3 smaller than the experimental value and 20 Å^3 smaller than that obtained from DFT. In contrast, the iFF description closely matches the lattice volume predicted by DFT, although both the iFF and DFT structures yield slightly larger volumes than those observed experimentally.

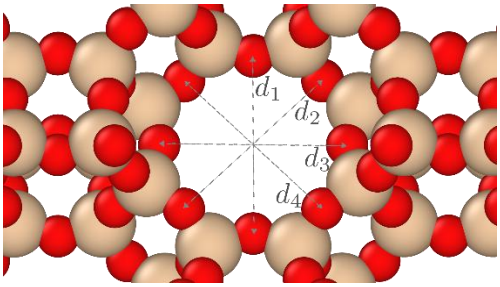


Figure S6: Chabazite aperture window showing distances between opposite oxygen atoms. Oxygen atoms are shown in red, and silicon atoms in beige.

Beyond the lattice parameters, the geometry of the chabazite aperture window is crucial for the description of the diffusion. Since the window is not planar, simple parameters such as radius or area are insufficient. Instead, the distances between pairs of opposite oxygen atoms were

measured to assess the accessibility of the aperture window. These distances are illustrated in Figure S6, and their values are summarized in Table S4. A clear observation is that the distances d2 and d4 are approximately equal, which arises from the geometry of the chabazite framework. In contrast, the distances d1 and d3 differ slightly. While these distances are nearly identical in the experimental structure, the theoretically optimized structures exhibit a larger disparity (approximately 0.3–0.4 Å). This indicates that the aperture window is not circular but slightly elliptical in shape.

Table S4: Distances between opposite oxygen atoms in the chabazite aperture window at 0 K for different methods: iFF and SLC force fields, DFT[9], IZA structure[10], and experimental published data[1]. Calculated structures ordered by increasing volume.

	d_1 (Å)	d_2 (Å)	d_3 (Å)	d_4 (Å)
SLC	6.375	6.873	6.695	6.873
iFF	6.284	6.903	6.552	6.903
DFT	6.226	6.849	6.623	6.849
IZA	6.354	6.951	6.627	6.951
exp	6.390	6.871	6.401	6.871

Temperature-induced flexibility

Temperature- and pressure-induced effects play a significant role in determining the structural behavior of porous materials, particularly their cell volume. In some zeolites, including CHA, a phenomenon known as thermal contraction is observed, where the unit cell volume decreases with increasing temperature.[11] Importantly, both force fields and the machine-learnt potential used in this study can reproduce this trend, as illustrated in Figure S7, where the volume of the chabazite reduced unit cell decreases systematically with temperature.

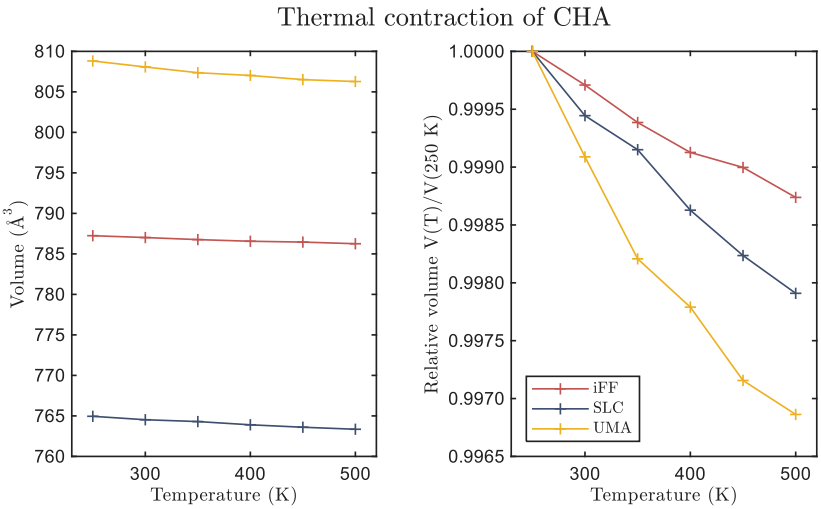


Figure S7: Temperature-induced effect on chabazite: thermal contraction. Cell volume at various temperatures (250–500 K) for two force fields – iFF (in orange) and SLC (in blue).

The thermal expansion coefficient quantifies how the volume of a material changes as a function of temperature. As CHA is nearly isotropic, the expansion coefficient can be calculated using relation:

$$a = \frac{a_V}{3} = \frac{1}{3V}\left(\frac{\mathrm{d}V}{\mathrm{d}T}\right)_p \quad (2)$$

The thermal expansion coefficient of CHA was calculated at 300 K under constant pressure. The resulting calculated coefficients are $a_{CHA,\ iFF}$ = −2.0 10^{-6} K^{-1}, $a_{CHA,\ SLC}$ = −2.8 10^{-6} K^{-1}, and $a_{CHA,\ UMA}$ = −6.0 10^{-6} K^{-1}. These values overestimate the experimentally reported coefficient at 298 K, which is $a_{CHA,\ exp}$ = −0.5 10^{-6} K^{-1}, but reproduce the decreasing trend. However, the experimentally reported coefficient is itself strongly temperature-dependent, ranging in magnitude from approximately −0.5 10^{-6} to −16.7 10^{-6} K^{-1} across the interval from 298 K to 873 K. All three calculated coefficients (−2.0 to −6.0 10^{-6} K^{-1}) fall within this experimentally observed range, suggesting that the apparent discrepancy at 298 K may reflect a shift in the effective temperature at which the simulations best reproduce the experimental behavior, rather than a genuine overestimation of the thermal contraction.

Guest-induced flexibility

Potential-energy barriers provide a static reference for the activated cage-to-cage hopping. They therefore provide insight into both host–guest interaction and the guest-induced framework flexibility involved in the activated hop. Potential energy barriers for cage-to-cage diffusion across the 8MR window were computed at 0 K using CI-NEB with iFF and SLC and compared against DFT as a higher-level energetic reference (see **Chyba! Nenalezen zdroj odkazů.** in the main text). Across the hydrocarbon series, iFF predicts systematically larger barriers than SLC. Relative to DFT, SLC tends to underestimate barriers, whereas iFF tends to overestimate them; the largest discrepancies occur for the slowest-diffusing molecules in the experimental ranking. Here, the guest-induced structural changes of the 8MR window are discussed further.

To study the structural impact of guest molecules, the geometry of the chabazite aperture window was analyzed. The distances between opposite oxygen atoms were used, see Figure S6. In this case, the distances were measured in configurations where the molecule is located at the transition state – i.e., passing through the 8-MR window. Transition state structures were obtained using the CI-NEB method for a series of C_1–C_4 hydrocarbons, using both iFF and SLC force fields, as well as the density functional theory. The absolute distance values as well as the values normalized to the distances in the corresponding empty framework structures are presented in Table S5.

The iFF models covalent interactions using harmonic potential only, resulting in a relatively stiff and less flexible framework. This rigidity is reflected in the small relative deformations observed; for example, the largest deviation (2.96 %) is found for the d_3 distance in (Z)-but-2-ene. However, most changes remain below 1 %. The most profound changes are for d_1 and d_3, the two axes of the ellipse.

In contrast, the SLC force field, which applies explicit restraints only to angles (and not to bonds), produces a more flexible framework. The maximum deviation, again for d_3 in (Z)-but-2-ene, reaches 4.09 %, and more values exceed the 1 % threshold. DFT calculations reveal even greater flexibility: the d_3 distance for the same molecule shows a deformation close to 10 %, and many other distances exhibit deviations greater than 1 %.

Table S5: Absolute values (in Å) and relative changes (in %) of distances between opposite oxygen atoms in the chabazite aperture window at 0 K using iFF, SLC, and DFT.

iFF	d_1	d_2	d_3	d_4	$\Delta_r d_1$	$\Delta_r d_2$	$\Delta_r d_3$	$\Delta_r d_4$
empty	6.284	6.903	6.552	6.903	0.00	0.00	0.00	0.00
but-1-ene	6.348	6.950	6.668	6.950	1.02	0.68	1.77	0.68
butane	6.349	6.965	6.679	6.943	1.03	0.90	1.94	0.58
(Z)-but-2-ene	6.325	6.898	6.746	7.032	0.65	-0.07	2.96	1.87
ethane	6.350	6.928	6.585	6.928	1.05	0.36	0.50	0.36
ethene	6.343	6.924	6.581	6.924	0.94	0.30	0.44	0.30
methane	6.344	6.924	6.583	6.924	0.95	0.30	0.47	0.30
propane	6.347	6.942	6.678	6.965	1.00	0.56	1.92	0.90
propene	6.335	6.937	6.644	6.943	0.81	0.49	1.40	0.58
(E)-but-2-ene	6.334	6.944	6.639	6.931	0.80	0.59	1.33	0.41

SLC	d_1	d_2	d_3	d_4	$\Delta_r d_1$	$\Delta_r d_2$	$\Delta_r d_3$	$\Delta_r d_4$
empty	6.375	6.873	6.695	6.873	0.00	0.00	0.00	0.00
but-1-ene	6.542	6.943	6.749	6.860	2.62	1.02	0.81	-0.19
butane	6.455	6.906	6.855	6.902	1.25	0.48	2.39	0.42
(Z)-but-2-ene	6.423	6.901	6.969	6.922	0.75	0.41	4.09	0.71
ethane	6.456	6.888	6.732	6.884	1.27	0.22	0.55	0.16
ethene	6.448	6.885	6.723	6.882	1.15	0.17	0.42	0.13
methane	6.448	6.883	6.719	6.883	1.15	0.15	0.36	0.15
propane	6.478	6.868	6.826	6.940	1.62	-0.07	1.96	0.97
propene	6.464	6.872	6.782	6.917	1.40	-0.01	1.30	0.64
(E)-but-2-ene	6.451	6.907	6.797	6.877	1.19	0.49	1.52	0.06

DFT	d_1	d_2	d_3	d_4	$\Delta_r d_1$	$\Delta_r d_2$	$\Delta_r d_3$	$\Delta_r d_4$
empty	6.226	6.849	6.623	6.849	0.00	0.00	0.00	0.00
but-1-ene	6.668	6.746	6.984	6.856	7.10	-1.50	5.45	0.10
butane	6.360	6.963	6.926	7.003	2.15	1.66	4.57	2.25
(Z)-but-2-ene	6.400	6.812	7.279	6.855	2.79	-0.54	9.90	0.09
ethane	6.519	6.778	6.838	6.782	4.71	-1.04	3.25	-0.98
ethene	6.544	6.776	6.890	6.776	5.11	-1.07	4.03	-1.07
methane	6.527	6.761	6.873	6.762	4.83	-1.28	3.77	-1.27
propane	6.418	6.941	6.946	6.939	3.08	1.34	4.88	1.31
propene	6.482	6.787	7.111	6.801	4.11	-0.91	7.37	-0.70
(E)-but-2-ene	6.483	6.797	7.131	6.799	4.13	-0.76	7.67	-0.73

Not all structural changes are positive across the different methods. For iFF, almost all deviations are positive, indicating that the window expands in all directions to adapt to the guest molecule. In contrast, the behavior under SLC becomes more complex. This more flexible force field allows the window to slightly contract in one direction while expanding in another, although only a single distance (d_2 or d_4) contracts. The effect becomes even more pronounced in the DFT results, where both d_2 and d_4 are more often contracted than expanded. For the majority of molecules, both distances simultaneously contract, allowing the opposite distances (d_1 and d_3) to stretch more substantially. This leads to an anisotropic deformation, in which the window elongates along the

shorter axes while contracting along the longer axes, effectively reshaping the aperture window to facilitate molecular passage through the framework.

This deformation also reveals a breaking of symmetry in the chabazite window. As mentioned in section with geometry-induced flexibility, distances d_2 and d_4 are approximately equal in the empty framework. Although small, symmetric molecules like methane (under all methods) and ethene or ethane (under iFF) preserve this equivalence, larger and less symmetric molecules lead to anisotropic deformations, breaking the equivalence between d2 and d4. For example, in (Z)-but-2-ene for iFF, d_2 slightly contracts while d_4 expands significantly (difference between the two is in about 0.13 Å). This symmetry breaking appears earlier and more severely under SLC and DFT than under iFF. This indicates that for these tightly fitting molecules, the window must be deformed, since the simple expansion of the window is not sufficient.

Overall, the passage of guest molecules through the chabazite window is consistently related to structural deformation. While these changes are often on the order of a few percent, some can approach 10 %, especially in DFT. This confirms that guest-induced framework flexibility plays a non-negligible role in diffusion and should be considered in any realistic simulation. Rigid or frozen framework approaches, traditionally used for computational simplicity, fail to capture these local relaxations, and thus risk misestimating diffusion coefficients.

Alongside energy barriers, interaction and deformation energies were also computed. The interaction energy is defined as the energy difference between the supersystem (zeolite plus probe molecule) and the sum of the separately optimized subsystems. The deformation energy is defined as the energy difference between the relaxed and deformed geometries of the subsystems.

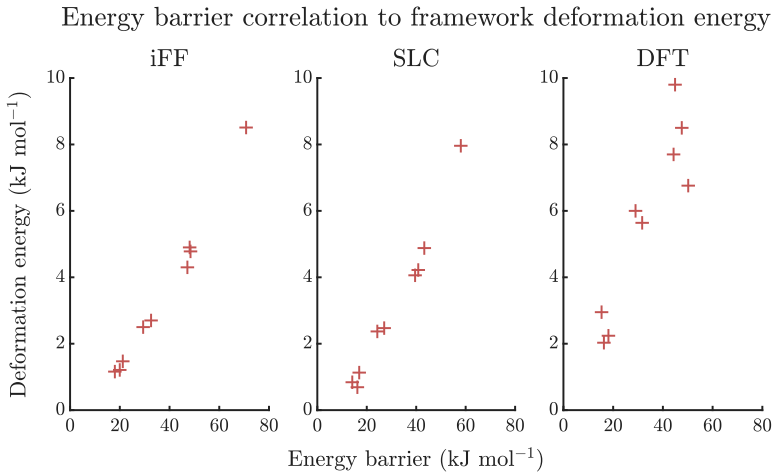


Figure S8: Correlation between energy barriers and framework deformation energies (kJ mol^{-1}) for different methods – iFF, SLC, and DFT.

The relationship between framework deformation and energy barriers is clear. As shown in Figure S8, there is a strong correlation between the energy barrier and the deformation energy of the framework at the transition state. For all methods, an increasing trend is observed, although the nature of the correlation varies. iFF exhibits the steepest dependence, where smaller deformation energies correspond to higher barriers, reflecting its relatively rigid framework description. In SLC, which provides a slightly softer framework, higher deformation energies are associated with higher barriers. Finally, DFT, the most flexible description, allows for larger framework deformations while maintaining relatively lower energy barriers. This again highlights

the critical role of framework flexibility in controlling diffusion and emphasizes the need for a dynamic and realistic description of the host structure.

Transferability to other methods

The same correction concept can also be used to test models outside the classical force-field family. Machine-learning interatomic potentials can make long-time simulations closer to electronic-structure accuracy, but their reliability near diffusion transition states still requires validation. This is particularly important for narrow-pore zeolites, where small errors in transition-state energetics can change predicted diffusion coefficients by orders of magnitude.

As an exploratory extension, the correction scheme was also tested for methane using UMA, a universal machine-learning interatomic potential. The simulations were performed using ASE.[12] The chosen general machine-learning interatomic potential was UMA s1.1 OMat model.[13] For methane, UMA gives a barrier of 24.2 kJ mol^{-1}, compared with 19.7 and 15.6 kJ mol^{-1} for iFF and SLC, respectively, and 16.3 kJ mol^{-1} from DFT. Thus, UMA does not automatically improve the transition-state energetics despite its greater model training and parameter flexibility.

However, after applying the DFT-based correction, the methane diffusion coefficients obtained with UMA, iFF, and SLC converge to similar values as presented in Figure 9. This single-adsorbate test suggests that the correction concept may be applicable beyond classical force fields, although broader testing across adsorbates and frameworks is required before making a general transferability claim.

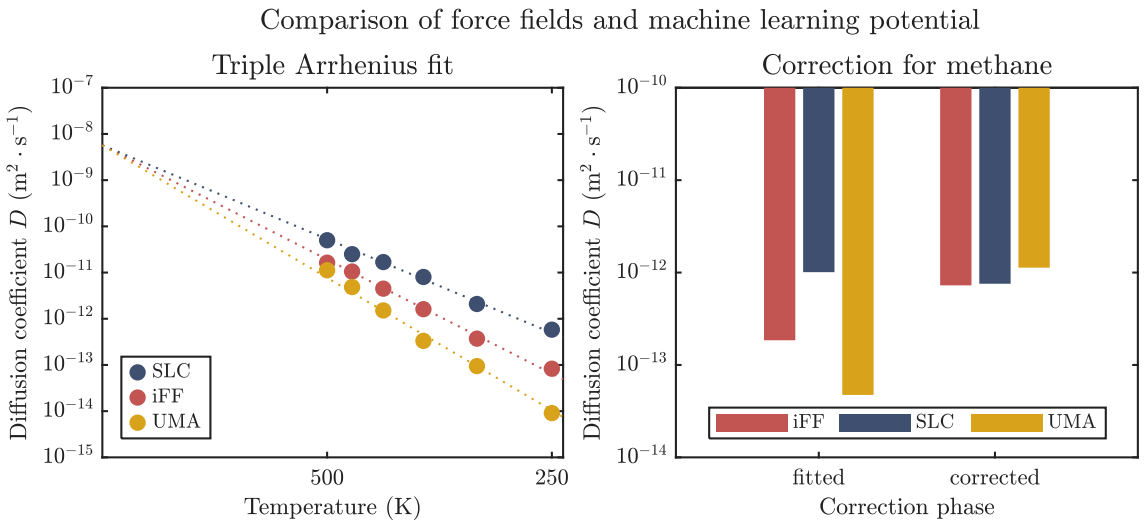


Figure S9: Left: Arrhenius fits of methane diffusion coefficients obtained with iFF, SLC, and UMA. Right: Diffusion coefficients at 300 K before and after correction, showing convergence across all three models.

References

(1) Díaz-Cabañas, M.-J.; A. Barrett, P. Synthesis and structure of pure SiO2 chabazite: the SiO2 polymorph with the lowest framework density. *Chemical Communications* **1998**, (17), 1881–1882.
(2) Miyamoto, M.; Nakatani, T.; Fujioka, Y.; Yogo, K. Verified synthesis of pure silica CHA-type zeolite in fluoride media. *Microporous and Mesoporous Materials* **2015**, *206*, 67–74.
(3) Petříček, V.; Dušek, M.; Palatinus, L. Crystallographic Computing System JANA2006: General features. *Zeitschrift für Kristallographie - Crystalline Materials* **2014**, *229* (5), 345–352.
(4) Thommes, M.; Kaneko, K.; Neimark, A. V.; Olivier, J. P.; Rodriguez-Reinoso, F.; Rouquerol, J.; Sing, K. S. W. Physisorption of gases, with special reference to the evaluation of surface area and pore size distribution (IUPAC Technical Report). *Pure and Applied Chemistry* **2015**, *87* (9-10), 1051–1069.
(5) Lippens, B. C.; de Boer, J. H. Studies on pore systems in catalysts: V. The t method. *Journal of Catalysis* **1965**, *4* (3), 319–323.
(6) Harkins, W. D.; Jura, G. Surfaces of Solids. XIII. A Vapor Adsorption Method for the Determination of the Area of a Solid without the Assumption of a Molecular Area, and the Areas Occupied by Nitrogen and Other Molecules on the Surface of a Solid. *Journal of the American Chemical Society* **1944**, *66* (8), 1366–1373.
(7) Jura, G.; Harkins, W. D. A New Adsorption Isotherm Which Is Valid Over a Very Wide Range of Pressure. *The Journal of Chemical Physics* **1943**, *11* (9), 430–431.
(8) Kärger, J. Determination of Diffusion Coefficients in Porous Media. In *Handbook of Heterogeneous Catalysis*, 2008; pp 1714–1727.
(9) Trachta, M.; Rubeš, M.; Bludský, O. Toward accurate ab initio modeling of siliceous zeolite structures. *The Journal of Chemical Physics* **2022**, *156* (9).
(10) Baerlocher, C.; Brouwer, D.; Marler, B.; McCusker, L. *Database of Zeolite Structures*. (accessed 2026).
(11) Woodcock, D. A.; Lightfoot, P.; Villaescusa, L. A.; Díaz-Cabañas, M.-J.; Camblor, M. A.; Engberg, D. Negative Thermal Expansion in the Siliceous Zeolites Chabazite and ITQ-4: A Neutron Powder Diffraction Study. *Chemistry of Materials* **1999**, *11* (9), 2508–2514.
(12) Hjorth Larsen, A.; Jørgen Mortensen, J.; Blomqvist, J.; Castelli, I. E.; Christensen, R.; Dułak, M.; Friis, J.; Groves, M. N.; Hammer, B.; Hargus, C.; et al. The atomic simulation environment—a Python library for working with atoms. *Journal of Physics: Condensed Matter* **2017**, *29* (27), 273002.
(13) Wood, B. M.; Dzamba, M.; Fu, X.; Gao, M.; Shuaibi, M.; Barroso-Luque, L.; Abdelmaqsoud, K.; Gharakhanyan, V.; Kitchin, J. R.; Levine, D. S.; et al. UMA: A Family of Universal Models for Atoms. 2026.